

Effect of N, C and B interstitials on the structural and magnetic properties of alloys with Cu_3Au -structure

Ingo Opahle^{1,*}, Harish K. Singh¹, Jan Zemen^{2,3}, Oliver Gutfleisch¹, and Hongbin Zhang¹

¹ *Institute of Materials Science, TU Darmstadt, 64287 Darmstadt, Germany*

² *Faculty of Electrical Engineering, Czech Technical University in Prague, Technická 2, Prague 166 27, Czech Republic*

³ *Department of Physics, Blackett Laboratory, Imperial College London, London SW7 2AZ, United Kingdom*

(Dated: October 22, 2021)

High-throughput density functional calculations are used to investigate the effect of interstitial B, C and N atoms on 21 alloys reported to crystallize in the cubic Cu_3Au structure. It is shown that the interstitials can have a significant impact on the magneto-crystalline anisotropy energy (MAE), the thermodynamic stability and the magnetic ground state structure, making these alloys interesting for hard magnetic, magnetocaloric and other applications. For 29 alloy/interstitial combinations the formation of stable alloys with interstitial concentrations above 5% is expected. In Ni_3Mn interstitial N induces a tetragonal distortion with substantial uniaxial MAE for realistic N concentrations. Mn_3XN_x ($X=\text{Rh, Ir, Pt}$ and Sb) are identified as alloys with strong magneto-crystalline anisotropy. For Mn_3Ir we find a strong enhancement of the MAE upon N alloying in the most stable collinear ferrimagnetic state as well as in the non-collinear magnetic ground state. Mn_3Ir and Mn_3IrN show also interesting topological transport properties. The effect of N concentration and strain on the magnetic properties are discussed. Further, the huge impact of N on the MAE of Mn_3Ir and a possible impact of interstitial N on amorphous Mn_3Ir , a material that is indispensable in today's data storage devices, are discussed at hand of the electronic structure. For Mn_3Sb , non-collinear, ferrimagnetic and ferromagnetic states are very close in energy, making this material potentially interesting for magnetocaloric applications. For the investigated Mn alloys and competing phases, the determination of the magnetic ground state is essential for a reliable prediction of the phase stability.

I. INTRODUCTION

Magnetic materials with a large magnetocrystalline anisotropy energy (MAE) are an important component in a wide range of everyday devices. Permanent magnets are used, for example, in hard disks, electro motors and direct drive wind turbines. Antiferromagnetic compounds find applications in exchange biased films for data storage devices, magnetic random access memories (MRAMs) and are of interest for spintronics applications [1–3]. Present high performance magnets like Nd-Fe-B contain a considerable amount of rare-earth elements, which in the past years have been subject to strong price fluctuations. The development of alternative permanent magnets without the use of critical rare-earth elements is therefore highly important [4–6]. Basic requirements for a good permanent magnet material are a large uniaxial magnetocrystalline anisotropy energy (MAE), a large saturation magnetization and a high Curie temperature.

High-throughput calculations in the framework of density functional theory (DFT) have become an increasingly important tool for the design of new functional materials in the past years [7, 8]. In addition to increased computational resources, this is due to the development of large databases and new concepts like efficient descriptors. A number of studies have focussed on the development of improved materials for batteries [9, 10], thermo-

electricity [11–13] or photovoltaics [14].

For magnetic materials, despite their technological importance, computational high-throughput studies are scarce. Bocarsly *et al.* performed a screening of potential magnetocaloric materials [15], and Elsässer *et al.* performed a screening of potential hard magnetic rare earth lean compounds [16–18]. Other studies focussed on potential rare earth free permanent magnets [19–22] or the prediction of new magnetic compounds [23–26]. A complete study of the stability, magnetic properties and MAE of potential new magnetic compounds taking into account competing phases and magnetic structures was to the best of our knowledge not performed up to now.

Theoretical high-throughput descriptions of functional magnetic materials involve different energy scales like Coulomb correlations, exchange interactions or magnetocrystalline anisotropy. Antiferromagnetic (AF) order can have a strong impact on the total energy and phase stability of Mn alloys [24, 27], which are of interest for hardmagnetic [28], magnetocaloric [29] as well as spintronics applications [2]. The effect of AF interactions on the energetics has been explored in high-throughput calculations for certain classes of compounds with known magnetic structure prototypes [24, 30, 31] or on selected compounds using evolutionary algorithms [25, 32] or a symmetry based prioritization [33]. Complex (non-collinear) structures and non-ferromagnetic ground states of competing structures in a phase diagram haven't been studied up to now, as the computational effort is easily enlarged by one order of magnitude, and often suitable magnetic structure prototypes are not known. For the calculation of the MAE, which sets an upper limit

* opahle@tmm.tu-darmstadt.de

to the coercivity, a proper treatment of spin-orbit coupling (SOC) and a high numerical accuracy, especially a careful convergence of k-space integrals are essential. Rare earth compounds with localized 4f electrons require a careful treatment of Coulomb correlations, where accurate methods suitable for a high-throughput screening still have to be developed. While individual aspects have been carefully addressed in the literature, the complexity of interactions makes a high-throughput prediction of functional magnetic materials still highly demanding.

It has been shown in the literature that interstitials can have a strong impact on the magnetic properties, including the magneto-crystalline anisotropy energy [34–36], the magnetic structure [37] and magnetostructural phase transitions [38, 39]. The Cu_3Au -structure is one of the most common structure types with more than 200 reported compounds. Ferromagnetic compounds like Fe_3Pt can exhibit a large magnetization, which makes them interesting for applications in exchange coupled magnets [40, 41]. Due to the cubic symmetry they have however only a relatively small MAE. In contrast, anti-ferromagnetic compounds like Mn_3Ir can exhibit a huge magneto-crystalline anisotropy [42], but have vanishing magnetization. This is used in exchange biased films, where giant exchange anisotropies are reported [43, 44]. Further, Mn-rich alloys of Cu_3Au -prototype have attracted attention due to a large magnetostriction [45] and Berry curvature related phenomena like a large anomalous Hall effect and a facet-dependent spin Hall effect [46–48].

In this article, we investigate the effect of interstitial N, C and B atoms on the stability and magnetic properties of 21 experimentally reported compounds with cubic Cu_3Au -structure and the magnetic 3d elements Cr, Mn, Fe, Co, and Ni. To identify the magnetic ground state of Mn alloys, the energy of different spin structures with maximal magnetic subgroup symmetry is calculated, which according to Ref. 49 accounts for the majority of measured magnetic structures on the Bilbao Crystallographic Server. This allows to identify also complex non-collinear (NC) ground states, which are frequently observed in Mn alloys. In total, about 1000 magnetic configurations are probed to obtain reliable energies for alloys relevant for the phase stability of binary and ternary Mn alloy systems related to this study (Fig.1). Stable interstitial phases are identified taking into account all possible decomposition reactions. We show that interstitials can lead to a strong enhancement of the magneto-crystalline anisotropy energy in these alloys and that high-throughput DFT calculations are able to identify hard magnetic materials even in the presence of complex magnetic interactions.

II. COMPUTATIONAL DETAILS

Calculations were performed within density functional theory using an extended version of the high-throughput

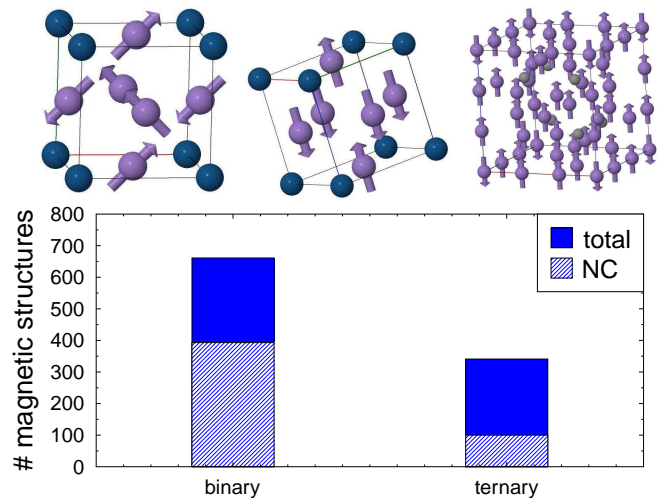


FIG. 1. Total number (filled blue) and number of NC (shaded blue) magnetic structures calculated for binary and ternary Mn alloys in this work. Some examples for automatically generated initial spin structures are shown as well: a non-collinear structure and collinear ferrimagnetic structure for Mn_3Ir and a collinear ferrimagnetic structure for Mn_{23}C_6 (from left to right).

environment HTE [50, 51] employing the VASP [52, 53] and FPLO [54] codes. For the present investigation, the HTE has been extended for the calculation of magnetic properties such as the investigation of different spin configurations and the calculation of the magneto-crystalline anisotropy energy (MAE). Further, an automatic detection of suitable interstitial positions was implemented.

For structure optimizations and the calculation of formation energies the VASP code [52, 53] has been used following a similar approach as in Ref. 51. For the final results shown here PAW pseudopotentials with a cut-off energy $E=500$ eV and constant density of k-points corresponding e.g. to a k-mesh of $14 \times 14 \times 14$ k-points in the full Brillouin zone (FBZ) for Mn_3Sb were used. For MAE calculations, the full potential local orbital method [54] (FPLO, version 14-49) was used, employing the optimized crystal and (collinear) magnetic structure obtained in the preceding VASP calculations. In the FPLO code, accurate full potential calculations are combined with the solution of the 4-component Kohn-Sham-Dirac equation, which implicitly contains spin-orbit coupling up to all orders.

As a descriptor for hard magnetic alloys the magnetic force theorem with a moderate k-mesh (up to $20 \times 20 \times 20$ k-points in the FBZ) was used, where starting from a selfconsistent scalar relativistic calculation, the MAE is evaluated in one-step calculations as the band energy difference between different magnetization directions. In addition, selfconsistent relativistic calculations with up to $32 \times 32 \times 32$ k-points in the FBZ were used to check the MAE for hard magnetic alloys identified in this study. Further, the magnetic anisotropy of $\text{Mn}_3\text{Ir}(\text{N})$ and

Mn₃Pt(N) in the non-collinear ground state was calculated using the VASP code employing the magnetic force theorem. Here, a cut-off energy $E=400$ eV and a k-mesh of $12 \times 12 \times 12$ k-points in the FBZ were used.

The results have been cross checked with selfconsistent calculations including spin-orbit coupling using a cut-off energy $E=500$ eV and k-meshes of $25 \times 25 \times 25$ k-points (Mn₃IrN) and $13 \times 13 \times 13$ k-points (Mn₃PtN), showing a convergence of the anisotropy energy of about 1 meV.

The anomalous Hall conductivity (AHC) is determined by using the WannierTools (WT) code, which is implemented within the framework of tight binding (TB) models [55]. The maximally localized Wannier functions (MLFWs) TB models are obtained by using the Wannier90 code [56]. We considered the s, p and d orbitals for Mn and Ir atoms, and s plus p orbitals were incorporated for N, resulting in 72 and 80 MLFWs for Mn₃Ir and Mn₃IrN respectively. To evaluate the AHC, the Berry curvature integration is carried out using a uniform kpoints mesh of $401 \times 401 \times 401$, which is expressed as following: [57]

$$\sigma_{xy} = -\frac{e^2}{\hbar} \int \frac{d\mathbf{k}}{(2\pi)^3} \sum_n f[\epsilon(\mathbf{k}) - \mu] \Omega_{n,xy}(\mathbf{k}) \quad (1)$$

$$\Omega_{n,xy}(\mathbf{k}) = -2\text{Im} \sum_{m \neq n} \frac{\langle \psi_{\mathbf{k}n} | v_x | \psi_{\mathbf{k}m} \rangle \langle \psi_{\mathbf{k}m} | v_y | \psi_{\mathbf{k}n} \rangle}{[\epsilon_m(\mathbf{k}) - \epsilon_n(\mathbf{k})]^2} \quad (2)$$

where e is elementary charge, μ is the chemical potential, $\psi_{n/m}$ denotes the Bloch wave function with energy eigenvalue $\epsilon_{n/m}$, $v_{x/y}$ is the velocity operator along Cartesian x/y direction, and $f[\epsilon(\mathbf{k}) - \mu]$ is the Fermi-Dirac distribution function. In this work, the ANC α_{xy} is determined by using the Mott relation, where we considered only the derivative of AHC at the Fermi level $d\sigma_{xy}/d\epsilon$, which provides a quantitative measure of the ANC.

$$\alpha_{xy} = -\frac{\pi^2 k_B^2 T}{3e} \left. \frac{d\sigma_{xy}}{d\epsilon} \right|_{\epsilon=\mu} \quad (3)$$

Unless otherwise mentioned, the generalized gradient approximation (GGA) in the parameterization of Perdew, Burke and Ernzerhof [58] was used. For calculations in the local spin density approximation (LSDA), which often provides a better description of the spin magnetic moments for weakly correlated systems, the parameterization of Perdew and Wang [59] is used.

For the detection of suitable interstitial positions, the unit cell is scanned on a discrete mesh (here $24 \times 24 \times 24$ points) for sufficient empty space, taking into account the covalent radii r_j of the atoms as tabulated in the Atomic Simulation Environment (ASE) [60, 61]. As condition for suitable positions for the interstitial I we use $d_{\min} = \min_j (d_{Ij} - s(r_I + r_j)) > 0$ for all neighbouring atoms j , where $s = 0.7$ is a scaling factor and d_{Ij} is the distance between the interstitial and the atom j . This approach is similar to the detection of empty spheres used in some electronic structure codes. Preference can be

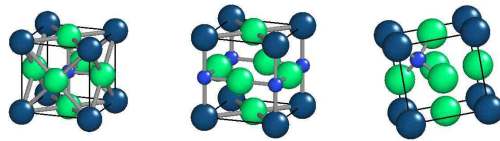


FIG. 2. Interstitial positions in the Cu₃Au-structure: 1b, 3d and 8g (from left to right).

given to high symmetry positions, which was done for the present calculations. The resulting interstitial positions for the Cu₃Au structure are shown in Fig. 2. The interstitial concentration was varied using $2 \times 2 \times 2$, $1 \times 2 \times 2$ and $1 \times 1 \times 1$ supercells with one interstitial position occupied, corresponding to interstitial concentrations of 3.0, 5.9, 11.1 and 20 at.%. An additional slight orthorhombic distortion (2-5% change of the lattice parameters) of the interstitial supercells was also tested, but did not have an effect on the stable interstitial compounds discussed in this manuscript.

The calculation of convex hulls is based on about 2000 alloys (experimental structures and structures close to the convex hull reported in the Materials Project [62]) for ternary M - X - Z systems (M =Fe, Co, Ni, Cr and Mn; Z =B, C, N; X : other element). For the competing phases, the same numerical setup as for the interstitial compounds was used. For compounds with Mn atoms, where antiferromagnetic couplings are to be expected, the magnetic ground state was determined for the parent compounds with Cu₃Au-structure and their stable interstitial alloys. To ensure reliable phase diagrams for the Mn systems, the magnetic ground state was also determined for the experimentally reported competing phases and some of the energetically low lying phases reported in the Materials Project. Depending on the size and symmetry of the cell, we used spin configurations compatible with the maximal magnetic subgroups with propagation vector $\mathbf{q}=(0,0,0)$, $(1/2,1/2,0)$, $(0,0,1/2)$ or alternatively an antiferromagnetic coupling of sublattices to probe the magnetic ground state.

In case of Mn₃Ir with Cu₃Au-prototype this results (after removal of symmetry equivalent configurations) in three collinear (FM, AF and ferrimagnetic) and one non-collinear initial spin structures for $\mathbf{q}=(0,0,0)$, which is sufficient to obtain the experimentally reported ground state. It is noteworthy that the experimentally reported magnetic structure of Mn₃Ir does not have maximal magnetic subgroup symmetry, but is compatible with the symmetry of the second generation of maximal subgroups (maximal subgroup $R3m'$ (#166.101) of the maximal subgroup $Pm\bar{3}m'$ (#221.95)). Nevertheless, the NC initial structures relax to the correct ground state, which underpins the high efficiency of the approach. We explicitly checked that the second generation of maximal subgroups results in the same magnetic ground state. The AF coupling of sublattices corresponds to the highest

| alloy | $a_{\text{exp}}[\text{\AA}]$ | $a_{\text{GGA}}[\text{\AA}]$ | $E_f[\text{eV/at.}]$ | $\Delta E_h[\text{eV/at.}]$ | $M[\mu_B/\text{f.u.}]$ |
|--------------------|------------------------------|------------------------------|----------------------|-----------------------------|------------------------|
| Co ₃ Al | 3.66 | 3.57 | -0.175 | 0.124 | 3.86 |
| Co ₃ Ta | 3.65 | 3.63 | -0.241 | 0.001 | 0.02 |
| Co ₃ Ti | 3.62 | 3.60 | -0.257 | 0.000 | 2.71 |
| Fe ₃ Ga | 3.70 | 3.66 | -0.133 | 0.000 | 6.98 |
| Fe ₃ Ge | 3.68 | 3.63 | -0.099 | 0.010 | 6.37 |
| Fe ₃ Pt | 3.77 | 3.73 | -0.076 | 0.041 | 8.46 |
| Fe ₃ Sn | 3.87 | 3.82 | 0.086 | 0.088 | 6.94 |
| Mn ₃ Ir | 3.77 | 3.71 | -0.215 | 0.000 | 0.01* |
| Mn ₃ Pt | 3.84 | 3.74 | -0.251 | 0.000 | 0.00* |
| Mn ₃ Rh | 3.81 | 3.71 | -0.142 | 0.000 | 0.00* |
| Mn ₃ Sb | 4.00 | 3.91 | 0.076 | 0.086 | 0.04* |
| Ni ₃ Fe | 3.55 | 3.55 | -0.088 | 0.000 | 4.72 |
| Ni ₃ Ga | 3.58 | 3.59 | -0.289 | 0.000 | 0.79 |
| Ni ₃ Ge | 3.57 | 3.57 | -0.292 | 0.000 | 0.05 |
| Ni ₃ In | 3.75 | 3.75 | -0.052 | 0.045 | 0.69 |
| Ni ₃ Mn | 3.59 | 3.56 | -0.102 | 0.000 | 4.85 |
| Ni ₃ Si | 3.51 | 3.51 | -0.462 | 0.000 | 0.04 |
| Ni ₃ Sn | 3.74 | 3.74 | -0.188 | 0.000 | 0.06 |
| Pt ₃ Co | 3.83 | 3.88 | -0.061 | 0.000 | 2.91 |
| Pt ₃ Cr | 3.88 | 3.91 | -0.254 | 0.000 | 2.60 |
| Rh ₃ Cr | 3.79 | 3.78 | -0.122 | 0.000 | 1.24 |

TABLE I. Properties of parent compounds in Cu₃Au-structure. Experimental (a_{exp}) and calculated lattice parameters (a_{GGA}), the calculated formation energy E_f and distance from the convex hull ΔE_h and the total magnetic moment M are shown. Non-collinear magnetic structures are marked with *.

ranked magnetic structures in the prioritization scheme proposed in Ref. 33 and is especially useful when the paramagnetic structure has a relatively large number of inequivalent magnetic atoms N_{AF} which are allowed to couple AF. The number of possible magnetic configurations at this prioritization level is $2^{N_{\text{AF}}-1}$, which results for instance for Mn₇C₃ of hexagonal Cr₇C₃,hP80,186-prototype (with 56 Mn atoms in the unit cell and $N_{\text{AF}} = 8$) in 128 possible magnetic configurations. While this approach does not ensure that the correct magnetic ground state is found in all cases, we believe it should give a reliable basis for the prediction of the phase stability in these systems. For the remaining alloys a ferromagnetic magnetic configuration was assumed.

III. RESULTS OF HIGH-THROUGHPUT SCREENING

A. Parent compounds in Cu₃Au-structure

Tab. I shows the calculated properties of the 21 parent compounds with Cu₃Au structure. The calculated lattice parameters are in good agreement with the reported experimental values, with the largest deviation of about 2.6% for Mn₃Rh and Mn₃Pt. With exception of Mn₃Sb and Fe₃Sn the calculated formation energy is negative for all compounds, as expected from formation of alloys in nature. Mn₃Sb has only been recently synthesized by high pressure synthesis [63] and the Cu₃Au-structure

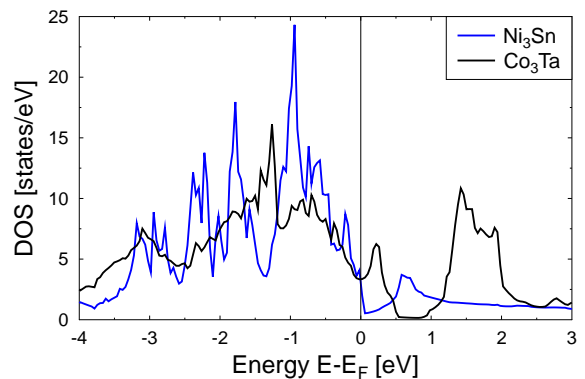


FIG. 3. Total DOS of Co₃Ta and Ni₃Sn for the experimental lattice parameters calculated with FPLO using GGA.

of Fe₃Sn was reported in high pressure studies, whereas the ambient pressure phase is hexagonal, in agreement with our calculations (see Supplementary). For 18 of the 21 compounds the calculated distance from the convex hull ΔE_h is below 50 meV/atom, which has been proposed in Ref. 51 as a simple descriptor for potentially stable or meta stable alloys in high-throughput calculations. In addition to the above mentioned Mn₃Sb and Fe₃Sn alloys, only Co₃Al is above this criterion, which shows the largest $\Delta E_h = 124$ meV/atom among the calculated compounds. A Cu₃Au-structure of Co₃Al has been discussed in the literature, but could not be stabilized experimentally [64]. This result is confirmed by our study, where only the Al rich phases AlCo, Al₅Co₂, Al₁₃Co₄, and Al₉Co₂ are found to be stable. A complete list of the alloys relevant for the calculation of the convex hull in Tab. I is given in the supplementary material.

For Ni₃X ($X=\text{Si, Ge, Sn}$) and Co₃Ta the Fermi energy lies in a pseudo gap or valley of the density of states (DOS), see Fig. 3, resulting in a non-magnetic or only weakly ferromagnetic ground state despite the presence of the magnetic elements Ni and Co. For Mn₃X ($X=\text{Rh, Ir, Pt}$ and Sb) the calculated ground state is non-collinear. The antiferromagnetic coupling of the neighbouring Mn atoms can not be fully satisfied in the Cu₃Au structure, resulting in a frustrated triangular spin structure with compensated magnetic moments, see for instance Ref. 42 for a more detailed discussion. For $X=\text{Rh, Ir, Pt}$ this result is in agreement with experiment [65, 66] and earlier calculations [42]. In case of Mn₃Pt a transition from a triangular to a collinear AF magnetic structure with a doubled unit cell along c was observed around 365 K in neutron scattering experiments [65], while a similar transition was not observed for Mn₃Rh and Mn₃Ir. For Mn₃Sb, the energies of NC, ferrimagnetic and ferromagnetic (FM) magnetic structures are within less than 35 meV/atom. Experimentally, a collinear magnetic structure with almost compensating Mn magnetic moments was deduced from neutron scattering experiments [67], while more recent Mössbauer studies suggest a triangular magnetic structure [68].

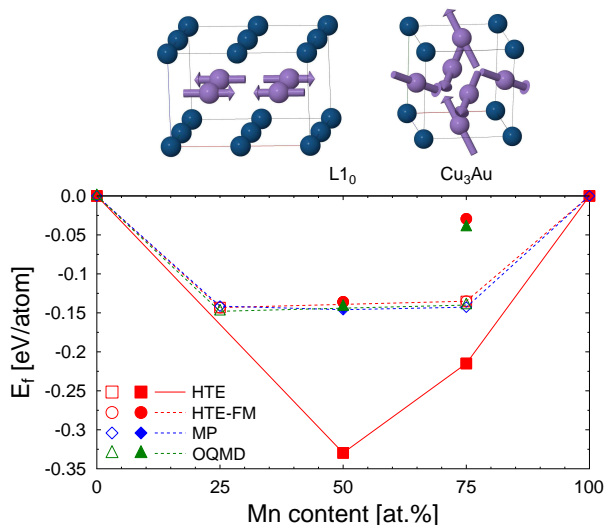


FIG. 4. Calculated formation energies (red squares) and convex hull (solid red line) for the magnetic ground state of Mn-Ir alloys. For comparison the convex hull (dashed lines) and formation energies obtained assuming a ferromagnetic structure from our calculations (red circles), the Materials Project (blue diamonds) and the Open Quantum Materials Database (green triangles) are shown. Formation energies for the experimentally reported $L1_0$ - and Cu_3Au -crystal structures obtained with the different calculation methods are plotted with filled symbols. Top: calculated magnetic groundstate structures for $MnIr$ and Mn_3Ir . Note that SOC was not included here and that the spin-quantization axis has been rotated to match the results of calculations with SOC.

The energy difference ΔE_{FM} between the magnetic ground state and a ferromagnetic state can be as large as 243 meV/atom for Mn_3Pt . For some of the competing phases the calculated ΔE_{FM} is of similar magnitude, while ΔE_{FM} is trivially zero for compounds with a ferromagnetic ground state. The magnetic structure can thus have a deep impact on the calculated phase stability, going beyond typical effects due to finite temperature. This is exemplarily shown in Fig. 4 for binary Mn-Ir alloys. Assuming a ferromagnetic spin alignment a hexagonal $MnIr_3$ phase, $L1_0$ - $MnIr$ and a hexagonal Mn_3Ir phase are on or nearly on the convex hull, in good agreement with results obtained from the Materials Project [62] and the Open Quantum Materials Database OQMD [69]. In contrast, calculations with the magnetic ground state yield the experimentally observed $L1_0$ - $MnIr$ and Cu_3Au -structure of Mn_3Ir as stable phases on the convex hull. For $L1_0$ - $MnIr$ and Cu_3Au - Mn_3Ir the magnetic ground state search resulted in a collinear AF and a NC triangular AF structure, respectively, in agreement with experiment [66, 70]. This is accompanied by a significant lowering of the formation energy of nearly 0.2 meV/atom. In contrast, the magnetic ground state search for the two (experimentally not observed) hexagonal phases did not have an effect on the calculated formation energy. A similar impact of the magnetic structure on the calculated

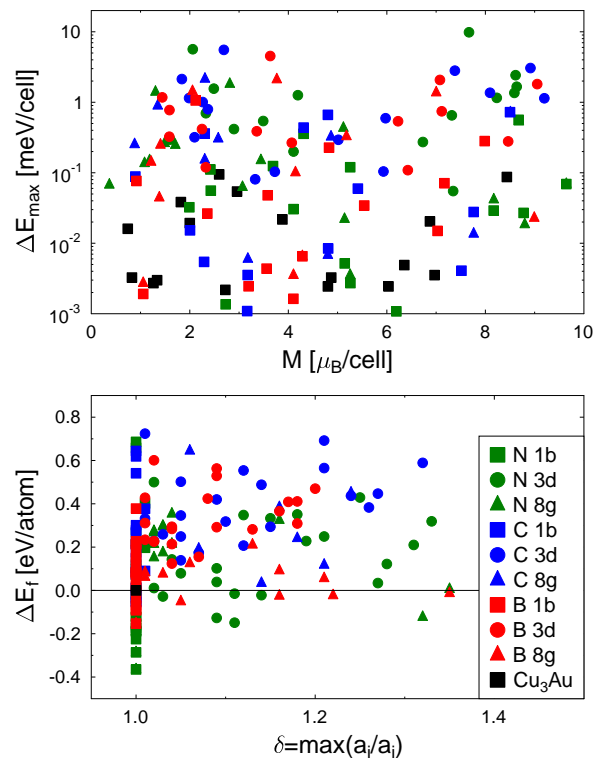


FIG. 5. Maximum energy difference $\Delta E_{\max} = \max(E_i - E_j)$ between different magnetization directions vs. total magnetic moment M (top) and maximal change of the ratio of lattice parameters $\delta = \max(a_i/a_j)$ vs. change in the formation energy ΔE_f (bottom). Data are shown for parent compounds in the Cu_3Au -structure (filled black squares) and interstitial structures with B (red), C (blue) and N (green). The interstitial 1b, 3d and 8g positions are marked with filled squares, circles and triangles, respectively.

phase stability as for Mn-Ir is found also in other Mn alloy systems and will be discussed in more detail elsewhere.

B. Effect of interstitials on structural and magnetic properties

Fig. 5 shows the calculated MAE (maximum energy difference between magnetization directions [001], [010], [100], [110], and [111]) for the Cu_3Au parent compounds and interstitial alloys with one N, C or B atom per f.u., assuming a ferromagnetic alignment of the spins. It can be seen that interstitials can induce huge MAEs up to about 2 meV/atom, one to two orders higher in magnitude than in their cubic parent compounds. N, C and B are similarly efficient in inducing these large MAEs. The largest MAEs are calculated for the 3d interstitial position, which leads to a tetragonal distortion of the lattice and therefore is promising to achieve uniaxial MAEs. There can be also a significant MAE between the [001], [110] and [111] directions of up to about 0.2 meV/atom

for the cubic compounds with heavy 5d elements (while the energy difference between [001], [010] and [100] is zero due to symmetry). It should be noted however, that neither stability nor potential antiferromagnetic spin configurations are considered in this plot. The MAEs shown in Fig. 5 thus rather serve to illustrate the potential of interstitials in inducing large MAEs, while for the majority of the data points an experimental realization will not be possible.

This becomes also clear from the lower plot of Fig. 5, which shows the formation energy difference ΔE_f with respect to the Cu_3Au parent compound in relation to the induced structural distortion for different interstitial atoms and positions. For the majority of data points ΔE_f is positive indicating that the interstitial alloy is unlikely to form, at least at the interstitial concentration of 20 at.% considered in the plot. Further, in most cases the 1b interstitial position, which does not break the cubic symmetry, is most stable. In most cases this means that a significant enhancement of the MAE is not expected. Noteworthy exceptions, where the spin structure breaks the cubic symmetry, will be discussed further below. Significant structural distortions are found for the 3d and 8g interstitial positions with negative ΔE_f in some cases, suggesting that the interstitial alloys are likely to form. For the 8g interstitial position, which is least favourable from geometrical considerations, we often find relaxation to a structure corresponding to the 1b or 3d position, which provide a higher volume for the interstitial atom.

C. Stable interstitial phases

Tab. II lists interstitial alloys, where the distance to the convex hull ΔE_h is below 50 meV/atom for an interstitial concentration of more than 5 at.%, suggesting that a substantial amount of interstitial atoms can be incorporated in the parent alloy with Cu_3Au -structure. This criterion is matched for 29 parent/interstitial combinations, including known antiperovskites like Mn_3XN ($X=\text{Rh}, \text{Ir}, \text{Pt}$ and Sb) [45, 71], Ni_3InN [72], Fe_3PtN [73], Co_3AlC [74], Fe_3GaC [75] and Fe_3SnN [76]. Only the most stable interstitial position is listed. In some cases more than one interstitial position lowers the formation energy, suggesting a partial occupation of the interstitial sites. This is for instance the case for Ni_3Mn , where the N 3d and 1b positions are close in energy and both of them fulfill the ΔE_h criterion for 5.9 at.% N concentration.

The largest gain in formation energy with respect to the parent compound $\Delta E_f \approx -0.3$ eV/atom is found for Mn_3SbN , where the 'interstitial' alloy [71] was reported more than 20 years before the meta stable 'parent' alloy Mn_3Sb [63]. For the majority of interstitial alloys, stability is accompanied by a negative ΔE_f . However, even a large negative ΔE_f does not ensure formation of a stable alloy. This is the case for instance for Co_3AlN and Co_3TiN , where the distance from the convex hull is

| parent | interst. | c_{\max} | E_f [eV/at.] | ΔE_h [eV/at.] | M [μ_B /at.] |
|------------------------|----------|------------|----------------|-----------------------|---------------------|
| Co_3Al | C 1b | 20.0 | -0.230 | 0.010 | 0.00 |
| Co_3Ta | B 1b | 11.1 | -0.272 | 0.044 | 0.00 |
| Co_3Ta | C 1b | 11.1 | -0.211 | 0.035 | 0.00 |
| Co_3Ti | B 1b | 11.1 | -0.324 | 0.043 | 0.31 |
| Co_3Ti | C 1b | 11.1 | -0.302 | 0.003 | 0.22 |
| Fe_3Ga | B 1b | 5.9 | -0.124 | 0.047 | 1.50 |
| Fe_3Ga | C 1b | 20.0 | -0.063 | 0.044 | 0.63 |
| Fe_3Ga | N 1b | 20.0 | -0.255 | 0.016 | 1.05 |
| Fe_3Ge | N 1b | 5.9 | -0.096 | 0.040 | 1.32 [†] |
| Fe_3Pt | N 1b | 20.0 | -0.263 | 0.000 | 1.63 |
| Fe_3Sn | N 1b | 20.0 | -0.104 | 0.037 | 1.02 |
| Mn_3Ir | N 1b | 20.0 | -0.359 | 0.026 | 0.00* |
| Mn_3Pt | N 1b | 20.0 | -0.471 | 0.000 | 0.00* |
| Mn_3Rh | N 1b | 20.0 | -0.356 | 0.000 | 0.00* |
| Mn_3Sb | N 1b | 20.0 | -0.226 | 0.036 | 0.55 [†] |
| Ni_3Fe | N 3d | 5.9 | -0.063 | 0.038 | 1.05 |
| Ni_3Ga | B 1b | 5.9 | -0.305 | 0.014 | 0.00 |
| Ni_3Ga | C 1b | 5.9 | -0.273 | 0.006 | 0.00 |
| Ni_3Ga | N 1b | 11.1 | -0.258 | 0.036 | 0.00 |
| Ni_3In | B 1b | 20.0 | -0.205 | 0.049 | 0.00 |
| Ni_3In | C 1b | 20.0 | -0.040 | 0.038 | 0.00 |
| Ni_3In | N 1b | 20.0 | -0.173 | 0.000 | 0.00 |
| Ni_3Mn | B 1b | 5.9 | -0.110 | 0.041 | 1.09 |
| Ni_3Mn | C 1b | 5.9 | -0.071 | 0.025 | 1.08 |
| Ni_3Mn | N 3d | 11.1 | -0.113 | 0.044 | 0.95 |
| Ni_3Sn | B 1b | 5.9 | -0.196 | 0.038 | 0.00 |
| Ni_3Sn | C 1b | 5.9 | -0.134 | 0.043 | 0.00 |
| Ni_3Sn | N 1b | 11.1 | -0.135 | 0.045 | 0.00 |
| Pt_3Co | B 8g | 11.1 | -0.069 | 0.048 | 0.59 |

TABLE II. Interstitial alloys with a distance from the convex hull $\Delta E_h < 50$ meV/atom. The parent compound with Cu_3Au -structure, the interstitial atom and position and the highest interstitial concentration c_{\max} with $\Delta E_h < 50$ meV/atom (with three different values of the interstitial concentrations: 5.9, 11.1 and 20) in at.% are shown along with the calculated formation energy E_f , ΔE_h and the total magnetic moment M per atom. Non-collinear magnetic structures and antiferromagnetic/ ferrimagnetic structures are indicated with * and [†], respectively.

0.3-0.4 eV/atom, despite ΔE_f values of about -0.16 and -0.13 eV/atom, respectively. Vice versa, a positive ΔE_f does not prevent the formation of a stable interstitial alloy, as in the case of Fe_3GaC_x .

For the majority of interstitials, the 1b position is energetically preferred. The 3d position, which is especially interesting for hard magnetic applications as it breaks the cubic symmetry and leads to a tetragonal distortion of the lattice, is energetically most preferable for Ni_3FeN_x , Ni_3MnN_x , $\text{Co}_3\text{Ta}_x\text{N}_x$ and $\text{Co}_3\text{Ti}_x\text{N}_x$. In all cases substantial MAEs between -0.67 and 1.3 meV/cell are induced for $x = 1$ (20 at.% N). The largest absolute value of 1.3 meV/cell is found for Ni_3MnN , albeit with an easy plane magnetization. However, for $\text{Co}_3\text{Ta}_x\text{N}_x$ and $\text{Co}_3\text{Ti}_x\text{N}_x$ only a minor amount of interstitials is expected to be incorporated due to the formation of extraordinary stable Ta-N and Ti-N phases (see Supplementary). For realistic N concentrations (11 at.% N, $x = 0.5$), Ni_3MnN_x shows a significant uniaxial MAE around -100 μeV /atom, com-

parable to hcp-Co. For Ni_3FeN_x , the MAE is small ($\approx 15 \mu\text{eV}/\text{atom}$) and depends on the choice of supercell.

Tab. III lists stable alloys with large uniaxial MAE for the most stable collinear magnetic structure obtained in the preceding VASP calculations. For comparison, also results obtained within LSDA (employing the same GGA optimized structure) are shown. For both GGA and LSDA, the listed alloys show a large uniaxial MAE, but the absolute values can differ significantly. While GGA typically yields lattice parameters in better agreement with experiment, the local spin magnetic moments are often better described within LSDA. As the MAE depends on subtle details of the electronic structure, this can have a strong impact on the calculated MAE [77], as is the case here for Mn_3Ir , Mn_3PtN and Mn_3SbN . According to the table, Mn_3XN and Mn_3X ($X=\text{Rh}$, Ir , Pt and Sb) would have a huge potential for application as hard magnets, provided they could be stabilized in a ferrimagnetic magnetic structure. The largest MAE of about $-1.3 \text{ meV}/\text{atom}$ is obtained for Mn_3IrN . Comparison with Tabs. I and II shows however that with exception of Mn_3SbN these large MAEs can not be readily used in bulk magnets, as the ground state is non-collinear with zero net magnetization. However, the strong MAE could be used in exchange coupled multilayer structures, where a hard magnetic antiferromagnetic layer is coupled to a soft magnetic layer with large magnetization and high Curie temperature. Moreover, as Mn_3SbN shows, a ferrimagnetic ground state may be induced either by variation of the interstitial concentration or epitaxial strain in a thin film. This will be further explored in Sec. IV.

Comparison of Tab. II and Tab. I shows some remarkable effects of the interstitials on the magnetic properties. While the ground states of Co_3Al is ferromagnetic, Co_3AlC is found to be non-magnetic. Similar, the total magnetic moment of Co_3Ti is strongly reduced by interstitial B, resulting in a non-magnetic ground state for (unstable) Co_3TiB . On the contrary, Co_3Ta is non-magnetic, while Co_3TaN would be magnetic if it could be synthesized. This shows that interstitials can be very efficient to tune magnetic transitions, which makes interstitial alloying interesting also for magnetocaloric applications.

IV. DISCUSSION

In the previous section we have shown that interstitial atoms can have a strong impact on the stability, magnetic properties and MAE of compounds. While in principle huge MAEs are possible (see Fig. 5), *stable* compounds with the necessary properties for a good permanent magnet are rare, in line with experimental experience. Among the 63 parent/interstitial combinations investigated in this study, Ni_3MnN_x with $x \approx 0.5$ was identified as a stable ferromagnetic alloy with magnetic properties comparable to hcp-Co at reduced cost. Further, Mn_3SbN was identified as a ferrimagnet with large MAE,

| alloy | interst. | $M_{\text{GGA}}/M_{\text{LSDA}}$ [μ_B/atom] | $\text{MAE}_{\text{GGA}}/\text{MAE}_{\text{LSDA}}$ [meV/atom] |
|-------------------------------|----------|---|--|
| Mn_3Ir | -- | $0.37^\dagger/0.30^\dagger$ | -0.19/-0.43 |
| Mn_3IrN | N 1b | $0.54^\dagger/0.49^\dagger$ | -1.32/-1.27 |
| Mn_3Pt | -- | $0.36^\dagger/0.32^\dagger$ | -0.09/-0.11 |
| Mn_3PtN | N 1b | $0.63^\dagger/0.57^\dagger$ | -0.16/-0.22 |
| Mn_3Rh | -- | $0.43^\dagger/0.37^\dagger$ | -0.10/-0.12 |
| Mn_3RhN | N 1b | $0.56^\dagger/0.51^\dagger$ | -0.31/-0.29 |
| Mn_3SbN | N 1b | $0.55^\dagger/0.52^\dagger$ | -0.20/-0.13 |
| $\text{Ni}_3\text{MnN}_{0.5}$ | N 3d | $0.96/0.90$ | -0.09/-0.10 |

TABLE III. Stable alloys with large uniaxial $\text{MAE}=E_{[001]} - E_{[100]}$. The total magnetic spin moment M and the MAE calculated within GGA/LSDA are listed. A collinear spin arrangement is assumed. Compounds with a ferrimagnetic structure are indicated with \dagger on the magnetic moment.

in agreement with a large magnetostriction observed experimentally in this compound [45]. It can be expected that an extended screening of more parent/interstitial combinations leads to even more promising candidates for hard magnetic applications.

The most striking observation in this study is however the huge MAE in Mn_3XN_x ($X=\text{Rh}$, Ir , Pt , and Sb) and the strong impact of interstitial N on the MAE in these compounds, especially for Mn_3IrN . Fig. 6 shows the calculated DOS of Mn_3IrN and Mn_3Ir . Interstitial N induces changes in the electronic structure in the range of a few hundred meV, larger than the changes in the electronic structure due to a change of the magnetization direction from the easy [001] axis to the hard [100] axis due to spin-orbit coupling, also shown for comparison in Fig. 6. The changes in the electronic structure lead also to a change of the orbital moment anisotropy of Ir ($\Delta\mu_l = 0.046\mu_B$ for Mn_3Ir ; $\Delta\mu_l = 0.073\mu_B$ for Mn_3IrN) and Mn ($\Delta\mu_l = 0.052\mu_B$ for Mn_3Ir ; $\Delta\mu_l = -0.085\mu_B$ for Mn_3IrN), which is closely related to the MAE. Thus, interstitial N has an impact on the electronic structure and MAE going far beyond structural distortions, in agreement with earlier investigations [36].

Another important observation is that according to our calculations the N concentration in Mn_3XN_x ($X=\text{Rh}$, Ir , Pt) can be varied in the range between 0-20 at.%, thus providing an additional tuning parameter for the MAE, see Fig. 7. In all cases the interstitial alloys are on or close to the convex hull, well below the $\Delta E_h < 50 \text{ meV}/\text{atom}$ criterion for (meta-) stability. However, a triangular spin structure is energetically preferred over the collinear ferrimagnetic structure throughout the whole concentration range. For Mn_3RhN_x , where the N 1b and 3d position lead to a gain in formation energy, more than 30 at.% interstitial N can be incorporated into the structure based on the ΔE_h criterion. For these high N concentrations a ferrimagnetic structure with significant net magnetization around $2 \mu_B/\text{f.u.}$ and MAE around $-1 \text{ meV}/\text{f.u.}$ is expected based on our calculations. A partial occupation of the N 1b and 3d interstitial positions may also explain deviations from an ideal triangular spin structure

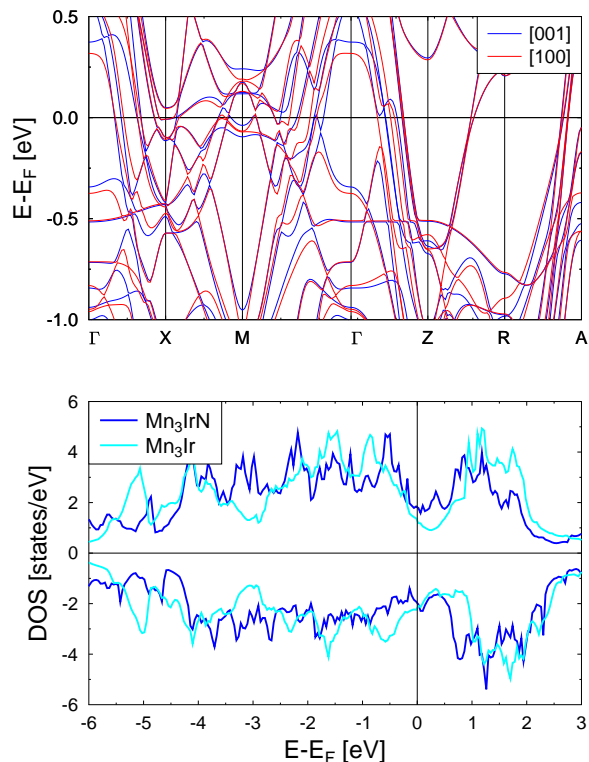


FIG. 6. Band structure (top) of ferrimagnetic Mn_3IrN for the easy [001] axis (blue) and the hard [100] axis (red). Comparison of the DOS of ferrimagnetic Mn_3IrN (blue) and ferromagnetic Mn_3Ir (cyan) for the easy [001] axis (bottom). For simplicity c/a in both graphs was set to 1.

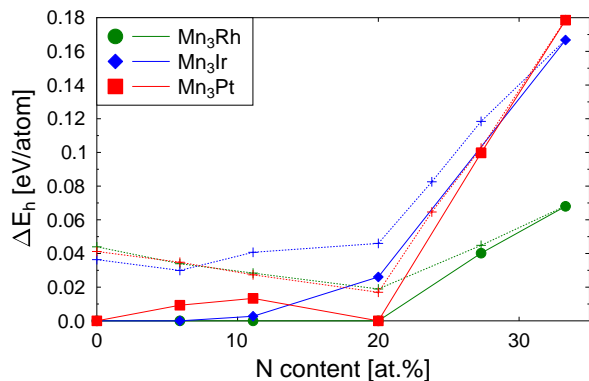


FIG. 7. Distance from convex hull ΔE_h vs. N concentration for Mn_3XN_x ($X=\text{Rh}, \text{Ir}, \text{Pt}$) (filled symbols: NC, plus: ferrimagnetic).

reported in this compound [71].

Fig. 8 shows the calculated MAE as a function of c/a for Mn_3IrN in the ferrimagnetic spin configuration employing selfconsistent calculations with an enhanced k-mesh. First, we note that the MAE obtained from selfconsistent calculations for the bulk value is in good agreement with the MAE obtained with the force theorem in the high-throughput calculations, underlining

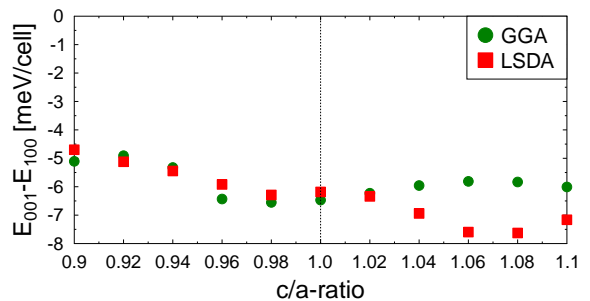


FIG. 8. Calculated MAE vs. c/a -ratio for Mn_3IrN . Results are shown for GGA (filled green circles) and LSDA (filled red squares). The volume was fixed to the GGA optimized bulk value.

the suitability of the band anisotropy as a descriptor in high-throughput calculations. The results show that the huge MAE is robust against variations of the c/a -ratio in epitaxially grown films, with values between -4 and -8 meV/cell for a wide range of lattice parameters. In particular, the results show that the symmetry breaking due to the ferrimagnetic spin arrangement is responsible for the huge MAE and not a slight distortion of the lattice from cubic symmetry ($c/a=1$). The total spin moment ranges between 2 and 4 μ_B/cell for c/a -ratios investigated. Thus, Mn_3IrN would be an excellent hard magnetic material if it could be stabilized in the ferrimagnetic spin configuration, which would outperform the known hard magnet $\text{L1}_0\text{-CoPt}$ with an MAE of about 0.5 meV/atom and a total magnetic moment of about 1.1 μ_B/atom . According to our VASP calculations, N has also a strong impact on the magnetic anisotropy in the NC ground state and enhances the energy difference $\Delta E = E_{\Gamma^{4g}} - E_{\Gamma^{5g}}$ between the easy Γ^{4g} ground state and the Γ^{5g} representation of the magnetic structure from about -8 meV (Mn_3Ir) to -12 meV (Mn_3IrN). Based on these results we expect that interstitial N has also a strong impact on amorphous Mn_3Ir , which is one of the state-of-the-art materials for providing exchange bias in hard magnetic films. In case of $\text{Mn}_3\text{Pt(N)}$, ΔE changes sign from -3 meV (Mn_3Pt) to 6 meV (Mn_3PtN), so that the Γ^{5g} representation becomes the ground state.

According to our calculations, a relatively large epitaxial strain around 5% is necessary to stabilize a ferrimagnetic ground state in Mn_3IrN at 0 K, see Fig. 1 in the Supplementary. Surprisingly, the necessary strain in Mn_3Ir is lower, despite the smaller energy difference between the NC and ferrimagnetic state in Mn_3IrN , possibly indicating that an intermediate N concentration is most suitable for a stabilization of the ferrimagnetic state. Further, we note that in the related compound Mn_3GaN calculations by Zemen *et al.* [78] have shown that a combination of strain and temperature leads to a stabilization of a ferrimagnetic ground state. A similar behaviour was recently also experimentally observed for a Mn_3NiN film on a SrTiO_3 substrate [79]. In passing we note also that epitaxial strain in Mn_3XN as well as

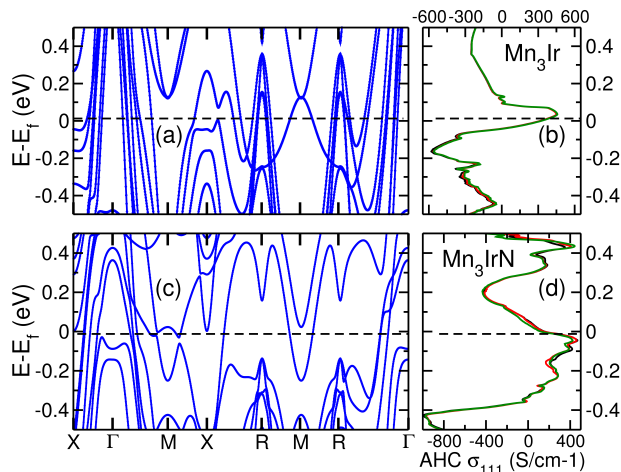


FIG. 9. Calculated band structure and AHC of Mn_3Ir [(a) and (b)] and Mn_3IrN [(c) and (d)] respectively. Fig. (b) and (d) the black, red and green line correspond to the σ_x and σ_y and σ_z AHC tensor.

in Mn_3X ($X=\text{Rh, Ir, Pt}$) is accompanied by a significant net magnetization in the NC ground state, albeit smaller than the one predicted for Mn_3SnN [80]. This suggests that a piezomagnetic effect may be observed in a wide range of NC antiferromagnets. A more detailed analysis is beyond the scope of the present high-throughput study and left for future experimental and theoretical work.

The anomalous Hall conductivity (AHC) and anomalous Nernst coefficient (ANC) depend on the spin configuration of the system. The origin of non-vanishing AHC in Γ_{4g} magnetic ordering has been studied based on symmetry analysis [81, 82]. Fig. 9 shows the calculated band structure and anomalous Hall conductivity (AHC) of Mn_3Ir and Mn_3IrN in the Γ_{4g} ground state. For both compounds, the calculated AHC σ_{111} is significant, with 315 S/cm for Mn_3Ir and 157 S/cm for Mn_3IrN . This is in overall good agreement with a study by Chen *et al.*, where a moderately smaller AHC was calculated for Mn_3Ir (230 S/cm) [46], but differs in sign and magnitude from a recent AHC calculation by Huyen *et al.* for Mn_3IrN (-573.3 S/cm) [83]. The AHC has been shown to be highly sensitive to the choice of the magnetization direction [82], which may be a reason for this discrepancy. Based on our calculations, we predict a huge anomalous Nernst effect, with calculated ANC α_{111} of 6195 and -4892 S/(cm eV) for Mn_3Ir and Mn_3IrN respectively. Noteworthy, there is change in sign of ANC for Mn_3IrN . Both end members of the Mn_3IrN_x ($0 \leq x \leq 1$) series show interesting transport properties. According to our thermodynamic calculations alloys with intermediate N concentrations are stable, which may be a route for further tuning of the transport properties.

V. SUMMARY

In summary we have shown that the interstitial elements N, C and B can have a strong impact on the magnetic properties of cubic compounds and that interstitial alloying can be a fruitful approach to enhance the magnetic properties. For reliable predictions of materials with enhanced properties, phase stability (i.e. calculation of the convex hull including all possible decomposition reactions) is essential. The high-throughput scheme introduced in this article is a unique computational tool to identify promising magnetic materials in order to guide the design of new magnetic materials.

Based on our calculations, we expect ferromagnetic Ni_3MnN_x (with about 11 at.% N) and the ferrimagnetic compounds Mn_3SbN and Mn_3RhN_x (with about 30 at.% N) to show bulk magnetic properties with sizable magnetization in the range of $0.5\text{-}1 \mu_B/\text{atom}$ and sizable uniaxial MAE in the range of $100\text{-}200 \mu\text{eV}/\text{atom}$.

The $\text{Mn}_3X(\text{N})$ ($X=\text{Rh, Ir, Pt}$ and Sb) compounds are identified as materials with strong MAE and a sizable magnetization in a collinear ferrimagnet state. The calculations also show that – with exception of Mn_3SbN – these materials can not readily be used as bulk magnets, as their ground state is a non-collinear fully compensated antiferromagnet. As a strong magnetic anisotropy is also present in the non-collinear ground state of these alloys, these materials are however of strong interest for multilayer structures where the hard magnetic antiferromagnetic layer is exchange coupled to a soft magnetic layer with large magnetization. Especially for Mn_3Ir , which is already used as exchange bias material in hard magnetic films, interstitial alloying with N can be a promising approach to enhance the magnetic properties of a state-of-the-art material. Further, an application of the strong MAE in the ferrimagnetic state may be possible in thin films, but requires more detailed theoretical and experimental investigations. For Mn_3Ir and Mn_3IrN we find a significant anomalous Hall effect and a huge anomalous Nernst effect. Variation of the N concentration may be a route for further optimization of the topological transport properties, as the Mn_3IrN_x alloys share the same triangular spin arrangement. Moreover, we have shown that interstitials can also have an impact on the ground state magnetic structure and can thus be used to tune magnetic transitions for instance in magnetocaloric applications. In $\text{Mn}_3\text{Sb}(\text{N})$ the magnetic ground state changes from NC to ferrimagnetic upon alloying with N. For Mn_3Sb , NC, ferrimagnetic and ferromagnetic magnetic states are very close in energy, indicating that moderate fields may be sufficient to switch from a low to a high magnetization state. This makes Mn_3Sb based alloys potentially interesting for magnetocaloric applications, but requires further studies.

For Mn alloys, our calculations show that the assumption of a ferromagnetic spin alignment, which is currently used in high-throughput databases, is unreliable to predict formation energies and phase stability. The symme-

try based methods applied in this article to determine the magnetic ground state can pave the way to predictions of the phase stability based on DFT-high-throughput calculations for these important alloy systems, which are of interest e.g. for permanent magnet, magnetocaloric and spintronics applications.

ACKNOWLEDGEMENTS

We acknowledge fruitful discussions with Karl G. Sandeman and Zsolt Gercsi. Financial support by the DFG CRC/TRR 270, the German federal state of Hes-

sen through its excellence programme LOEWE "RESPONSE" and the European Community (NOVAMAG) is gratefully acknowledged. The work of JZ was supported by the Ministry of Education, Youth and Sports of the Czech Republic from the OP RDE programme under the project International Mobility of Researchers MSCA-IF at CTU No. CZ.02.2.69/0.0/0.0/18.070/0010457, and from the Large Infrastructures for Research, Experimental Development and Innovations project IT4Innovations National Supercomputing Center-LM2015070. Calculations for this research were conducted on the Lichtenberg high performance computer of the TU Darmstadt.

-
- [1] D. Sander, S. O. Valenzuela, D. Makarov, C. H. Marrows, E. E. Fullerton, P. Fischer, J. McCord, P. Vavassori, S. Mangin, P. Pirro, B. Hillebrands, A. D. Kent, T. Jungwirth, O. Gutfleisch, C. G. Kim, and A. Berger, The 2017 magnetism roadmap, *Journal of Physics D: Applied Physics* **50**, 363001 (2017).
- [2] J. Železný, H. Gao, K. Výborný, J. Zemen, J. Mašek, A. Manchon, J. Wunderlich, J. Sinova, and T. Jungwirth, Relativistic Néel-Order Fields Induced by Electrical Current in Antiferromagnets, *Phys. Rev. Lett.* **113**, 157201 (2014).
- [3] V. Baltz, A. Manchon, M. Tsoi, T. Moriyama, T. Ono, and Y. Tserkovnyak, Antiferromagnetic spintronics, *Rev. Mod. Phys.* **90**, 015005 (2018).
- [4] O. Gutfleisch, M. A. Willard, E. Brück, C. H. Chen, S. G. Sankar, and J. P. Liu, Magnetic Materials and Devices for the 21st Century: Stronger, Lighter, and More Energy Efficient, *Adv. Mater.* **23**, 821 (2011).
- [5] M. D. Kuz'min, K. P. Skokov, H. Jian, I. Radulov, and O. Gutfleisch, Towards high-performance permanent magnets without rare earths, *J. Phys. Condens. Matter* **26**, 064205 (2014).
- [6] K. Skokov and O. Gutfleisch, Heavy rare earth free, free rare earth and rare earth free magnets - vision and reality, *Scr. Mater.* **154**, 289 (2018).
- [7] S. Curtarolo, G. L. W. Hart, M. B. Nardelli, N. Mingo, S. Sanvito, and O. Levy, The high-throughput highway to computational materials design, *Nat. Mater.* **12**, 191 (2013).
- [8] A. Jain, S. P. Ong, G. Hautier, W. Chen, W. D. Richards, S. Dacek, S. Cholia, D. Gunter, D. Skinner, G. Ceder, and K. A. Persson, Commentary: The Materials Project: A materials genome approach to accelerating materials innovation, *APL Mater.* **1**, 011002 (2013).
- [9] G. Hautier, A. Jain, S. P. Ong, B. Kang, C. Moore, R. Doe, and G. Ceder, Phosphates as Lithium-Ion Battery Cathodes: An Evaluation Based on High-Throughput ab Initio Calculations, *Chem. Mater.* **23**, 3495 (2011).
- [10] J. E. Saal, S. Kirklin, M. Aykol, B. Meredig, and C. Wolverton, Materials Design and Discovery with High-Throughput Density Functional Theory: The Open Quantum Materials Database (OQMD), *JOM* **65**, 1501 (2013).
- [11] G. K. H. Madsen, Automated Search for New Thermoelectric Materials: The Case of LiZnSb, *J. Am. Chem. Soc.* **128**, 12140 (2006).
- [12] S. Wang, Z. Wang, W. Setyawan, N. Mingo, and S. Curtarolo, Assessing the Thermoelectric Properties of Sintered Compounds via High-Throughput *Ab-Initio* Calculations, *Phys. Rev. X* **1**, 021012 (2011).
- [13] C. Bera, S. Jacob, I. Opahle, N. S. H. Gunda, R. Chmielowski, G. Dennler, and G. K. H. Madsen, Integrated computational materials discovery of silver doped tin sulfide as a thermoelectric material, *Phys. Chem. Chem. Phys.* **16**, 19894 (2014).
- [14] L. Yu and A. Zunger, Identification of Potential Photovoltaic Absorbers Based on First-Principles Spectroscopic Screening of Materials, *Phys. Rev. Lett.* **108**, 068701 (2012).
- [15] J. D. Bocarsly, E. E. Levin, C. A. C. Garcia, K. Schwenicke, S. D. Wilson, and R. Seshadri, A Simple Computational Proxy for Screening Magnetocaloric Compounds, *Chem. Mater.* **29**, 1613 (2017).
- [16] N. Drebov, A. Martinez-Limia, L. Kunz, A. Gola, T. Shigematsu, T. Eckl, P. Gumbsch, and C. Elsässer, Ab initio screening methodology applied to the search for new permanent magnetic materials, *New J. Phys.* **15**, 125023 (2013).
- [17] W. Körner, G. Krugel, and C. Elsässer, Theoretical screening of intermetallic ThMn12-type phases for new hard-magnetic compounds with low rare earth content, *Sci. Rep.* **6**, 24686 (2016).
- [18] W. Körner, G. Krugel, D. F. Urban, and C. Elsässer, Screening of rare-earth-lean intermetallic 1-11 and 1-11-X compounds of YNi9In2-type for hard-magnetic applications, *Scr. Mater.* **154**, 295 (2018).
- [19] A. Edström, J. Chico, A. Jakobsson, A. Bergman, and J. Rusz, Electronic structure and magnetic properties of $1/0$ binary alloys, *Phys. Rev. B* **90**, 014402 (2014).
- [20] H. C. Herper, Ni-based heusler compounds: How to tune the magnetocrystalline anisotropy, *Phys. Rev. B* **98**, 014411 (2018).
- [21] O. Y. Vekilova, B. Fayyazi, K. P. Skokov, O. Gutfleisch, C. Echevarria-Bonet, J. M. Barandiarán, A. Kovacs, J. Fischbacher, T. Schrefl, O. Eriksson, and H. C. Herper, Tuning the magnetocrystalline anisotropy of Fe_3Sn by alloying, *Phys. Rev. B* **99**, 024421 (2019).

- [22] B. Fayyazi, K. P. Skokov, T. Faske, I. Opahle, M. Duerrschabel, T. Helbig, I. Soldatov, U. Rohrmann, L. Molina-Luna, K. Gth, H. Zhang, W. Donner, R. Schfer, and O. Gutfleisch, Experimental and computational analysis of binary Fe-Sn ferromagnetic compounds, *Acta Mater.* **180**, 126 (2019).
- [23] S. Sanvito, C. Oses, J. Xue, A. Tiwari, M. Zic, T. Archer, P. Tozman, M. Venkatesan, M. Coey, and S. Curtarolo, Accelerated discovery of new magnets in the Heusler alloy family, *Science Advances* **3**, e1602241 (2017).
- [24] J. Balluff, K. Diekmann, G. Reiss, and M. Meiner, High-throughput screening for antiferromagnetic Heusler compounds using density functional theory, *Phys. Rev. Materials* **1**, 034404 (2017).
- [25] S. Arapan, P. Nieves, and S. Cuesta-López, A high-throughput exploration of magnetic materials by using structure predicting methods, *J. of Appl. Phys.* **123**, 083904 (2018).
- [26] H. K. Singh, Z. Zhang, I. Opahle, D. Ohmer, Y. Yao, and H. Zhang, High-Throughput Screening of Magnetic Antiperovskites, *Chem. Mater.* **30**, 6983 (2018).
- [27] J. Kübler, K. H. Höck, J. Sticht, and A. R. Williams, Density functional theory of non-collinear magnetism, *J. Phys. F* **18**, 469 (1988).
- [28] W. Zhang, P. Kharel, S. Valloppilly, L. Yue, and D. J. Sellmyer, High-energy-product mnbi films with controllable anisotropy, *Phys. Status Solidi B* **252**, 1934 (2015).
- [29] J. Liu, T. Gottschall, K. P. Skokov, J. D. Moore, and O. Gutfleisch, Giant magnetocaloric effect driven by structural transitions, *Nat. Mater.* **11**, 620 (2012).
- [30] D. Ohmer, I. Opahle, H. K. Singh, and H. Zhang, Stability predictions of magnetic M_2AX compounds, *J. Phys. Condens. Matter* **31**, 405902 (2019).
- [31] Q. Gao, I. Opahle, and H. Zhang, High-throughput screening for spin-gapless semiconductors in quaternary Heusler compounds, *Phys. Rev. Materials* **3**, 024410 (2019).
- [32] A. Payne, G. Avendao-Franco, E. Bousquet, and A. H. Rome ro, Firefly Algorithm Applied to Noncollinear Magnetic Phase Materials Prediction, *J. Chem. Theory and Comput.* **14**, 4455 (2018), pMID: 29966084.
- [33] M. K. Horton, J. H. Montoya, M. Liu, and K. A. Persson, High-throughput prediction of the ground-state collinear magnetic order of inorganic materials using Density Functional Theory, *Npj Comput. Mater.* **5**, 10.1038/s41524-019-0199-7 (2019).
- [34] J. Coey and H. Sun, Improved magnetic properties by treatment of iron-based rare earth intermetallic compounds in ammonia, *J. Magn. Magn. Mater.* **87**, L251 (1990).
- [35] L. Steinbeck, M. Richter, U. Nitzsche, and H. Eschrig, Ab initio calculation of electronic structure, crystal field, and intrinsic magnetic properties of Sm_2Fe_{17} , $Sm_2Fe_{17}N_3$, $Sm_2Fe_{17}C_3$, and Sm_2Co_{17} , *Phys. Rev. B* **53**, 7111 (1996).
- [36] H. Zhang, I. Dirba, T. Helbig, L. Alff, and O. Gutfleisch, Engineering perpendicular magnetic anisotropy in Fe via interstitial nitrogenation: N choose K, *APL Materials* **4**, 116104 (2016).
- [37] M. Gajdzik, C. Sürgers, M. Kelemen, and H. v. Löhneysen, Ferromagnetism in carbon-doped Mn_5Si_3 films, *J. Appl. Phys.* **87**, 6013 (2000).
- [38] J. Lyubina, O. Gutfleisch, M. D. Kuzmin, and M. Richter, $La(Fe,Si)_{13}$ -based magnetic refrigerants obtained by novel processing routes, *J. Magn. Magn. Mater.* **320**, 2252 (2008).
- [39] N. T. Trung, L. Zhang, L. Caron, K. H. J. Buschow, and E. Brück, Giant magnetocaloric effects by tailoring the phase transitions, *Appl. Phys. Lett.* **96**, 172504 (2010).
- [40] J. Lyubina, I. Opahle, K.-H. Müller, O. Gutfleisch, M. Richter, M. Wolf, and L. Schultz, Magnetocrystalline anisotropy in $L1_0$ FePt and exchange coupling in FePt/Fe₃Pt nanocomposites, *J. Phys. Condens. Matter* **17**, 4157 (2005).
- [41] N. Hai, N. Dempsey, and D. Givord, Hard magnetic FePt alloys prepared by cold-deformation, *J. Magn. Magn. Mater.* **262**, 353 (2003), special issue on the Occasion of the Hanoi International Symposium on Magnetism:Cryolab 25.
- [42] L. Szunyogh, B. Lazarovits, L. Udvardi, J. Jackson, and U. Nowak, Giant magnetic anisotropy of the bulk antiferromagnets IrMn and IrMn₃ from first principles, *Phys. Rev. B* **79**, 020403 (2009).
- [43] K.-i. Imakita, M. Tsunoda, and M. Takahashi, Giant exchange anisotropy observed in MnIr-CoFe bilayers containing ordered Mn₃Ir phase, *Appl. Phys. Lett.* **85**, 3812 (2004).
- [44] A. Kohn, A. Kovács, R. Fan, G. J. McIntyre, R. C. C. Ward, and J. P. Goff, The antiferromagnetic structures of IrMn₃ and their influence on exchange-bias, *Sci. Rep.* **3**, 2412 (2013).
- [45] T. Shimizu, T. Shibayama, K. Asano, and K. Takenaka, Giant magnetostriction in tetragonally distorted antiperovskite manganese nitrides, *J. Appl. Phys.* **111**, 07A903 (2012).
- [46] H. Chen, Q. Niu, and A. H. MacDonald, Anomalous Hall Effect Arising from Noncollinear Antiferromagnetism, *Phys. Rev. Lett.* **112**, 017205 (2014).
- [47] Z. Q. Liu, H. Chen, J. M. Wang, J. H. Liu, K. Wang, Z. X. Feng, H. Yan, X. R. Wang, C. B. Jiang, J. M. D. Coey, and A. H. MacDonald, Electrical switching of the topological anomalous Hall effect in a non-collinear antiferromagnet above room temperature, *Nat. Electron.* **1**, 172 (2018).
- [48] W. Zhang, W. Han, S.-H. Yang, Y. Sun, Y. Zhang, B. Yan, and S. S. P. Parkin, Giant facet-dependent spin-orbit torque and spin hall conductivity in the triangular antiferromagnet irmn₃, *Sci. Adv.* **2**, 10.1126/sciadv.1600759 (2016).
- [49] S. V. Gallego, J. M. Perez-Mato, L. Elcoro, E. S. Tasci, R. M. Hanson, K. Momma, M. I. Aroyo, and G. Madariaga, *MAGNDATA*: towards a database of magnetic structures. I.The commensurate case, *J. Appl. Crystallogr.* **49**, 1750 (2016).
- [50] I. Opahle, G. K. H. Madsen, and R. Drautz, High throughput density functional investigations of the stability, electronic structure and thermoelectric properties of binary silicides, *Phys. Chem. Chem. Phys.* **14**, 16197 (2012).
- [51] I. Opahle, A. Parma, E. J. McEniry, R. Drautz, and G. K. H. Madsen, High-throughput study of the structural stability and thermoelectric properties of transition metal silicides, *New J. Phys.* **15**, 105010 (2013).
- [52] G. Kresse and J. Furthmüller, Efficient iterative schemes for ab initio total-energy calculations using a plane-wave basis set, *Phys. Rev. B* **54**, 11169 (1996).

- [53] G. Kresse and D. Joubert, From ultrasoft pseudopotentials to the projector augmented-wave method, *Phys. Rev. B* **59**, 1758 (1999).
- [54] K. Koepernik and H. Eschrig, Full-potential nonorthogonal local-orbital minimum-basis band-structure scheme, *Phys. Rev. B* **59**, 1743 (1999).
- [55] Q. Wu, S. Zhang, H.-F. Song, M. Troyer, and A. A. Soluyanov, WannierTools : An open-source software package for novel topological materials, *Comput. Phys. Commun.* **224**, 405 (2018).
- [56] A. A. Mostofi, J. R. Yates, Y.-S. Lee, I. Souza, D. Vanderbilt, and N. Marzari, wannier90: A tool for obtaining maximally-localised Wannier functions, *Comput. Phys. Commun.* **178**, 685 (2008).
- [57] D. Xiao, M.-C. Chang, and Q. Niu, Berry phase effects on electronic properties, *Rev. Mod. Phys.* **82**, 1959 (2010).
- [58] J. P. Perdew, K. Burke, and M. Ernzerhof, Generalized Gradient Approximation Made Simple, *Phys. Rev. Lett.* **77**, 3865 (1996).
- [59] J. P. Perdew and Y. Wang, Accurate and simple analytic representation of the electron-gas correlation energy, *Phys. Rev. B* **45**, 13244 (1992).
- [60] S. R. Bahn and K. W. Jacobsen, An object-oriented scripting interface to a legacy electronic structure code, *Comput. Sci. Eng.* **4**, 56 (2002).
- [61] A. H. Larsen, J. J. Mortensen, J. Blomqvist, I. E. Castelli, R. Christensen, M. Duak, J. Friis, M. N. Groves, B. Hammer, C. Hargus, E. D. Hermes, P. C. Jennings, P. B. Jensen, J. Kermode, J. R. Kitchin, E. L. Kolsbjerg, J. Kubal, K. Kaasbjerg, S. Lysgaard, J. B. Maronsson, T. Maxson, T. Olsen, L. Pastewka, A. Peterson, C. Rostgaard, J. Schitz, O. Schtt, M. Strange, K. S. Thygesen, T. Vegge, L. Vilhelmsen, M. Walter, Z. Zeng, and K. W. Jacobsen, The atomic simulation environmenta Python library for working with atoms, *J. Phys. Condens. Matter* **29**, 273002 (2017).
- [62] <https://materialsproject.org>.
- [63] T. Yamashita, H. Takizawa, T. Sasaki, K. Uheda, and T. Endo, Mn_3Sb : a new $L1_2$ -type intermetallic compound synthesized under high-pressure, *J. Alloys Compd.* **348**, 220 (2003).
- [64] M. Ellner, S. Kek, and B. Predel, Zur existenz einer phase cu_3al vom cu_3au -strukturtyp, *J. Alloys Compd.* **189**, 245 (1992).
- [65] E. Krén, G. Kádár, L. Pál, J. Sólyom, P. Szabó, and T. Tarnóczy, Magnetic Structures and Exchange Interactions in the Mn-Pt System, *Phys. Rev.* **171**, 574 (1968).
- [66] I. Tomeno, H. N. Fuke, H. Iwasaki, M. Sahashi, and Y. Tsunoda, Magnetic neutron scattering study of ordered Mn_3Ir , *J. Appl. Phys.* **86**, 3853 (1999).
- [67] V. M. Ryzhkovskii, V. S. Goncharov, S. S. Agafonov, V. P. Glazkov, V. A. Somenkov, A. P. Sazonov, and A. T. Senishin, Magnetic ordering in Mn_3Sb determined by neutron diffraction data, *J. Synth. Investig.* **5**, 109 (2011).
- [68] M. Budzynski, V. S. Goncharov, V. I. Mitsiuk, Z. Surowiec, and T. M. Tkachenka, Mössbauer Study of Cubic Phase in the Mn-Sb System, *Acta Phys. Pol. A* **125**, 850 (2014), 41st Polish Seminar on Positron Annihilation (PSPA), Lublin, POLAND, SEP 09-13, 2013.
- [69] <http://oqmd.org/>.
- [70] K. Selte, A. Kjekshus, A. F. Andresen, and W. B. Pearson, Equiatomic Transition Metal Alloys of Manganese. VII. A Neutron Diffraction Study of Magnetic Ordering in the IrMn Phase., *Acta Chem. Scand.* **22**, 3039 (1968).
- [71] D. Fruchart and E. F. Bertaut, Magnetic Studies of the Metallic Perovskite-Type Compounds of Manganese, *J. Phys. Soc. Jpn.* **44**, 781 (1978).
- [72] W. Cao, B. He, C. Liao, L. Yang, L. Zeng, and C. Dong, Preparation and properties of antiperovskite-type nitrides: $InNNi_3$ and $InNCo_3$, *J. Solid State Chem.* **182**, 3353 (2009).
- [73] G. W. Wiener and J. A. Berger, Structure and Magnetic Properties of Some Transition Metal Nitrides, *JOM* **7**, 360 (1955).
- [74] L. Huetter and H. Stadelmaier, Ternary carbides of transition metals with aluminum and magnesium, *Acta Metall.* **6**, 367 (1958).
- [75] A. Houben, J. Burghaus, and R. Dronskowski, The Ternary Nitrides $GaFe_3N$ and $AlFe_3N$: Improved Synthesis and Magnetic Properties, *Chem. Mater.* **21**, 4332 (2009).
- [76] T. Scholz and R. Dronskowski, Improved Ammonolytic Synthesis, Structure Determination, Electronic Structure, and Magnetic Properties of the Solid Solution $Sn_xFe_{4-x}N$ ($0 \leq x \leq 0.9$), *Inorg. Chem.* **54**, 8800 (2015).
- [77] S. Ener, M. Fries, F. Hammerath, I. Opahle, E. Simon, P. Fritsch, S. Wurmehl, H. Zhang, and O. Gutfleisch, Magnetic and magnetocaloric properties of the $Co_{2-x}Mn_xB$ system by experiment and density functional theory, *Acta Mater.* **165**, 270 (2019).
- [78] J. Zemen, E. Mendive-Tapia, Z. Gercsi, R. Banerjee, J. B. Staunton, and K. G. Sandeman, Frustrated magnetism and caloric effects in Mn-based antiperovskite nitrides: Ab initio theory, *Phys. Rev. B* **95**, 184438 (2017).
- [79] D. Boldrin, F. Johnson, R. Thompson, A. P. Mihai, B. Zou, J. Zemen, J. Griffiths, P. Gubeljak, K. L. Ormandy, P. Manuel, D. D. Khalyavin, B. Ouladdiaf, N. Qureshi, P. Petrov, W. Branford, and L. F. Cohen, The Biaxial Strain Dependence of Magnetic Order in Spin Frustrated Mn_3NiN Thin Films, *Adv. Funct. Mater.* **29**, 1902502 (2019).
- [80] J. Zemen, Z. Gercsi, and K. G. Sandeman, Piezomagnetism as a counterpart of the magnetovolume effect in magnetically frustrated Mn-based antiperovskite nitrides, *Phys. Rev. B* **96**, 024451 (2017).
- [81] G. Gurung, D.-F. Shao, T. R. Paudel, and E. Y. Tsymbal, Anomalous hall conductivity of noncollinear magnetic antiperovskites, *Phys. Rev. Materials* **3**, 044409 (2019).
- [82] I. Samathrakakis and H. Zhang, Piezospintronic effect in antiperovskite Mn_3GaN , arXiv preprint arXiv:1905.11798 (2019).
- [83] V. T. N. Huyen, M.-T. Suzuki, K. Yamauchi, and T. Oguchi, Topology analysis for anomalous Hall effect in the noncollinear antiferromagnetic states of Mn_3AN ($A = Ni, Cu, Zn, Ga, Ge, Pd, In, Sn, Ir, Pt$), *Phys. Rev. B* **100**, 094426 (2019).